ADVANCED ENERGY MATERIALS

www.advenergymat.de

3D Nanowire Arrayed Cu Current Collector toward Homogeneous Alloying Anode Deposition for Enhanced Sodium Storage

Xiao-Yong Fan, Jiaxing Han, Yuan-Li Ding,* Ya-Ping Deng, Dan Luo, Xiangtian Zeng, Zhen Jiang, Lei Gou, Dong-Lin Li,* and Zhongwei Chen**

Alloying electrodes are regarded as promising anodes for lithium/sodium storage thanks to their multielectron reaction capacity, moderate voltage plateau, and high electrical conductivity. However, huge volume change upon cycling, especially for sodium storage, usually causes the loss of electrical connection between active components and their delaminations from traditional current collectors, thus leading to rapid capacity decay. Herein, a unique 3D current collector is assembled from 1D nanowire arrays anchored on 3D porous Cu foams for constructing core-shelled Cu@Sb nanowires as advanced sodium-ion battery (SIB) anodes. The so-formed hierarchical 3D anode with interconnected 3D micrometer sized pores and abundant voids between nanowires not only effectively accommodates the structural strains during repeated cycling but also ensures the structural integrity and contributes to a uniform ion/electron scattered distribution throughout the whole surface. When employed as anodes for SIBs, the obtained electrode shows a high capacity of 605.3 mAh g^{-1} at 330 mA g^{-1}, and demonstrates a high capacity retention of 84.8% even at a high current density of 3300 mA g^{-1}. The 3D nanowire arrayed Cu current collector in this work can offer a promising strategy for designing and building advanced alloy anodes for lithium/sodium storage.

1. Introduction

With the development of modern industries, the energy crisis is becoming one of the most urgent issues which need to be resolved in our life.[1] Therefore, exploration of sustainable and renewable energy from solar, wind, biomass power, etc., is considered to be the top priority.[2] Effective utilization of these energy demands highly efficient energy storage systems. Among these potential candidates, sodium-ion batteries (SIBs) have drawn much attention and gained fast development thanks to rich sodium resources and its low cost (\$135–165 per ton for Na_2CO_3 , which is only ≈3% of that of Li_2CO_3).[1d,2c,3] However, SIBs usually display lower capacities and shorter cycle life compared with lithium-ion batteries (LIBs) due to larger structural strain and volume changes upon sodiation/desodiation, especially for alloying anode.[4] Thus, it is highly necessary to probe efficient electrode materials those can well accommodate the large volume expansion/contraction upon cycling. To effectively address these issues, several strategies are generally employed, including 1) synthesis of special architectures, such as 3D porous structure, to reduce ion diffusion distance and accommodate volume changes,[5] 2) alloying with active or inactive elements to partially buffer volume changes,[6] 3) designing and building alloy/C composites to alleviate volume changes and structure stability,[7] 4) surface engineering to maintain structure stability through preventing the reaction between active materials and electrolyte during the repeated sodiation/desodiation process,[6d,8] and 5) synthesis of self-supported nanoarchitectured array structures to reduce electron and ion transfer distance meanwhile accommodate volume changes.[5b,8b,9]

Although the above various nanostructures can effectively mitigate the volume expansion effect of alloying anode at a material level, it is difficult for avoiding the delamination of active components from traditional flat Cu current collector owing to a large volume variation, which strongly rely on the uniform mixing process of the active materials, conductive

Prof. X.-Y. Fan, J. Han, X. Zeng, Z. Jiang, Prof. L. Gou, Prof. D.-L. Li
School of Materials Science and Engineering
Chang'an University
Xi'an 710061, China
E-mail: xyfan@chd.edu.cn; dlli@chd.edu.cn
Prof. Y.-L. Ding
College of Materials Science and Engineering
Hunan University
Hunan 410082, China
E-mail: ylding@hnu.edu.cn
Y.-P. Deng, D. Luo, Prof. Z. W. Chen
Department of Chemical Engineering
University of Waterloo
200 University Avenue West, Waterloo, ON N2L 3G1, Canada
E-mail: zhwchen@uwaterloo.ca
The ORCID identification number(s) for the author(s) of this article can be found under https://doi.org/10.1002/aenm.201900673.

DOI: 10.1002/aenm.201900673

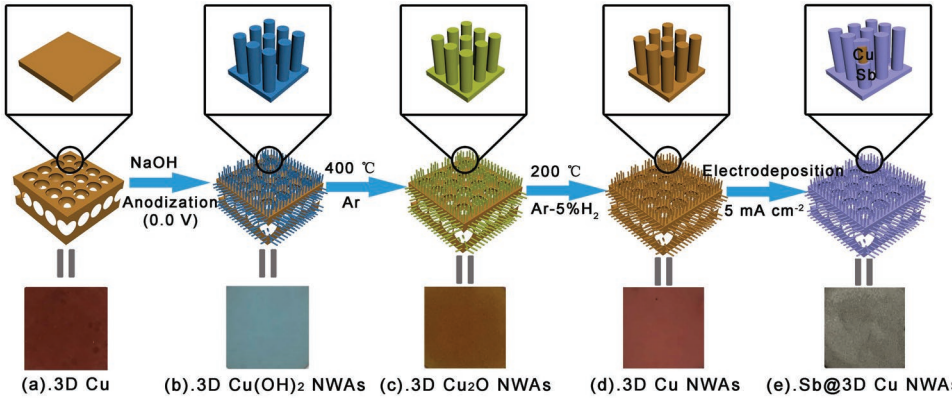

Figure 1. Schematic illustration of the preparation process of in situ growing Cu nanowire arrays on 3D porous Cu. a) 3D porous Cu. b) 3D $Cu(OH)_2$ NWAs. c) 3D Cu_2O NWAs. d) 3D Cu NWAs. e) Sb@3D Cu NWAs.

agent and binder, and their good interconnection with each other. In this context, developing nanoscale 3D current collector for constructing alloying anode will be an effective approach because it cannot only controllably construct nanoscale alloying anode but also achieve robust interconnection between active components and current collector at a nanoscale. In this work, we choose Sb as an alloying anode case for demonstrating such nanoscale 3D current collector in the use for SIBs since antimony (Sb) is considered to be one appealing candidate owing to its theoretical capacity reaches 660 mAh g^{-1} considered the reversible reaction $Sb + 3Na^+ \rightarrow Na_3Sb$, flat charge/discharge plateaus with moderate sodium intercalation/deintercalation potentials (≈0.8 V), and excellent electrical conductivity.[6b,10] However, Sb suffers remarkable volume changes (≈290%) during sodiation/desodiation, resulting in pulverization/exfoliation of Sb active particles and solid electrolyte interphase (SEI) film continuous growing.[6b,10a,11] It is expected that electrochemical properties of such 3D current collectors-based alloying anode would be simultaneously guaranteed at the both material level and electrode level.

Herein, we report an unique 3D current collector assembled from 1D nanowire arrays anchored on 3D porous Cu foams for constructing core-shelled Cu@Sb nanowires as advanced SIB anode. In this contribution, Cu nanowire arrays are grown on 3D porous Cu through anodizing and subsequent high-temperature reduction, as shown in **Figure 1**. First, the pore walls of 3D porous Cu (produced via an electroless plating, and the pore size is about 5 µm) are cover by $Cu(OH)_2$ nanowire arrays via anodizing (denoted as 3D $Cu(OH)_2$ NWAs). Then, 3D $Cu(OH)_2$ NWAs are heat treated under Ar and Ar-H_2 atmosphere subsequently to achieve Cu nanowire arrays anchored on 3D porous Cu (denoted as 3D Cu NWAs). Finally, a thin film of Sb is electrochemical deposited on 3D Cu NWAs and named as Sb@3D Cu NWAs. The macropores and voids between nanowire arrays in Sb@3D Cu NWAs electrode can offer rapid transfer channels for Na^+ and accommodate the volume changes during Na storage as well. Besides, the nanowire arrays can reduce the electron transfer distance as well. Under the synergetic effect of 3D porous structure and nanowire arrays, Sb@3D Cu NWAs electrode demonstrates an outstanding electrochemical performance when directly evaluated as a self-supported and binder-free electrode for sodium electrochemical storage. The reversible capacity has a high value of 605.3 mAh g^{-1} at 330 mAh g^{-1} and an ultrahigh retention of 92.7% (561.1 mAh g^{-1}) remained when suffered 200 cycles. Even cycled at a high current density of 3300 mA g^{-1}, Sb@3D Cu NWAs electrode displays a high capacity retention of 84.8% (554.6 mAh g^{-1}). Moreover, we also demonstrate the full cell performance of the as-prepared unique electrode, showing high energy density of 263 Wh kg^{-1}. Such findings manifest a great prospect of the proposed 3D current collector in practical battery or other related energy storage applications.

2. Results and Discussion

To enhance the sodium storage of element Sb as the anode for SIBs, Cu nanowire arrays anchored on 3D porous Cu (3D Cu NWAs) are constructed using anodizing for preparing 3D $Cu(OH)_2$ nanowire arrays (denoted as 3D $Cu(OH)_2$ NWAs) coupled with subsequent annealing and reduction. First, Linear sweep voltammetry (LSV) of 3D porous Cu in the electrolyte containing 0.3 M NaOH was carried out to determine the anodizing electrode potential for preparing 3D Cu nanowire arrays, and **Figure 2** shows the corresponding profiles. From

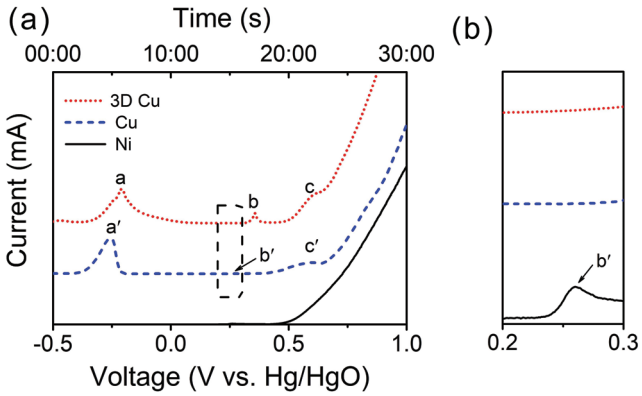

Figure 2. Linear sweep voltammetry (LSV) curves of the 3D porous Cu, Cu foil, and Ni foil in electrolytes containing 0.3 M NaOH, respectively. Each wave is labeled. Primes distinguish peak location and represent the same peak in for every LSV where present.

open circuit potential (–0.5 vs Hg/HgO) to –0.35 V, there is no current, indicating no electrode reaction (Figure 2a). Then, there appears an anodic peak *a* at –0.2 V, presenting the electrode reaction ($Cu + 2OH^{--} 2e^{-} \rightarrow Cu(OH)_2$) (Figure 2a). Besides, there appears an anodic peak at 0.35 V coupled with a shoulder peak at 0.6 V (Figure 2a). As shown from Video S1 in the Supporting Information (anodizing of 3D porous Cu at 0.6 V), there are a large number of bubbles releasing at 0.6 V, indicating O_2 formation. To better learn the involved electrochemical reactions during the anodizing process of 3D porous Cu, the LSV curves of Cu and Ni foils are also tested in the same condition. It can be observed that the anodizing peaks on Cu foil are similar to those on 3D porous Cu except there is no anodic peak at 0.35 V. The anodizing peaks of Cu foil show a little shift negatively, which can be attributed to its larger polarization because of smaller specific surface area. Observed from the LSV curve of Ni foil (Figure 2b), there appears an anodic peak at 0.26 V presenting oxidation Ni element. Compared with the LSV curve of Ni foil, the anodic peak of 3D porous Cu at 0.35 V maybe caused by the oxidation of Ni element, which comes from the production process of 3D porous Cu. According to the standard electrode potentials of $Cu(OH)_2$ and Cu_2O (Equations (1)–(3)) , the LSV curves of 3D porous Cu, the color changes (Video S2, Supporting Information, LSV of 3D porous Cu from open circuit to 1.0 V), there is almost no anodizing reaction at –0.3 V, Cu_2O formed at –0.2 V, $Cu(OH)_2$ formed at –0.1 and 0 V, CuO formed at 0.3 V (Equation (4)). There begins to release O_2 when the electrode potential increases to 0. 6 V (Equation (5)). Therefore we chose –0.3, –0.2, –0.1, and 0 V as the electrode anodizing electrode potentials to prepare 3D Cu nanowire arrays. Besides, we also chose 0.2, 0.6, and 1.0 V for comparison.

$$Cu_2O + H_2O + 2e \rightarrow 2Cu + 2OH^- \quad E^0 = -0.262\,V\,(\text{vs HgO/Hg}) \tag{1}$$

$$Cu(OH)_2 + 2e \rightarrow Cu + 2OH^- \quad E^0 = -0.124\,V\,(\text{vs HgO/Hg}) \tag{2}$$

$$2Cu(OH)_2 + 2e \rightarrow Cu_2O + 2OH^- + H_2O \quad E^0 = 0.018\,V\,(\text{vs HgO/Hg}) \tag{3}$$

$$Cu(OH)_2 + 2OH^- \rightarrow Cu(OH)_4^{2-} \rightarrow CuO + 2OH^- + H_2O \tag{4}$$

$$O_2 + 2H_2O + 4e \rightarrow {}^4OH^- \quad E^0 = 0.499\,V \tag{5}$$

Figure 3 gives the morphology of the samples prepared by anodizing at the electrode potential of –0.3, –0.2, –0.1, and 0 V (vs Hg/HgO) for 20 s coupled with subsequent high temperature treatment at 400 °C for 2 h in the flow of Argon atmosphere (possible reactions: $2Cu(OH)_2 \rightarrow 2CuO + 2H_2O\uparrow$, $Cu + CuO \rightarrow 2Cu_2O$) and reduction under H_2/Ar (5 vol%H_2) flow at 200 °C for 4 h ($Cu_2O + H_2 \rightarrow Cu + H_2\uparrow$).[12] As shown in Figure 3a–c, there is almost no morphology change on the 3D porous Cu surface after anodizing at –0.3 V compared with it before anodizing (Figure S1a,b, Supporting Information). The current versus time curve of 3D porous Cu anodized at –0.3 V (Figure S2, Supporting Information) shows there is very small current density, indicating low anodizing reaction rate, which leads to no nanowires growth. When the anodizing electrode potentials are set at –0.2 V (Figure 3d–f) and –0.1 V (Figure 3g–i), some Cu nanowires grow in the 3D porous Cu. However, the 3D porous structure is destroyed to some extent and a few larger cones appear due to large anodizing striping rate of Cu caused by large anodizing current (Figure S2, Supporting Information). The smaller anodizing current at –0.1 V compared with that at –0.2 V resulting in less destruction of Cu, thus the Cu nanowires achieved at –0.1 V are denser than those at –0.2 V. When the anodizing electrode potential is 0 V, the anodizing current is smaller than that at –0.1 V, which maybe more suitable for uniform nanowires growth. Thus, a large number of Cu nanowires uniformly distribute in the 3D porous Cu with the 3D porous structure remains well (Figure 3j–l). Cu nanowires show 150–200 nm in diameter and larger than 1 μm in length (Figure 3k). When the electrode potentials are 0.2, 0.6, and 1.0 V, there is no nanowire appears (Figure S3, Supporting Information). As shown in Figure 2a, there is no current at 0.2 V, which is also confirmed by the anodizing current show in Figure S2 in the Supporting Information. This phenomenon maybe attributed to the 3D porous Cu is rapidly passivated with dense CuO film deposited on its surface at high electrode potential of 0.2 V according to Equation (4) and Video S2 in the Supporting Information. Thus, Cu surface anodized at 0.2 V shows some destruction but with no nanowire appears (Figure S3a–c, Supporting Information). Similar to 0.2 V, the 3D porous Cu is also passivated rapidly with dense CuO film deposited on its surface at 0.6 V, meanwhile there are large number of O_2 bubbles release (see Video S2, Supporting Information), resulting in no morphology change appears compared with 3D porous Cu (Figure S3d–f, Supporting Information). When the electrode potential increases to 1.0 V, the dense CuO film on the surface of 3D porous Cu is also been resolved in the solution. Thus, the 3D porous Cu is destroyed again to some extent with large cones on the surface (Figure S3g–i, Supporting Information).

Based on above, the 3D porous Cu after anodizing at 0 V has the best architecture as the current collector for supporting electrode materials of lithium-ion or sodium-ion batteries. According to the current versus time curve of 3D porous Cu at 0 V (Figure S2, Supporting Information), the anodizing current density gradually decreases along with time and approaches 0 at 40 s. Thus, we chose 10 and 40 s for comparison. When the anodizing time is 10 s, the pore walls of 3D porous Cu are not fully grown by Cu nanowires (**Figure 4**a–c). When the anodizing time is 40 s, the 3D porous Cu are fully grown Cu nanowires, but the 3D porous structure is serious destroyed (Figure 4d–f).

Based above research results, we choose the 3D porous Cu after anodizing at 0 V for 20 s coupled with subsequent high temperature treatment and reduction (3D Cu NWAs) as the current collector for the Sb anode of SIBs. This unique 3D porous structure combined with nanowire arrays could be served as the most effective current collectors and frameworks for the direct and spontaneous supporting of the active materials, resulting in a high specific surface area and large numbers of activation sites. The well remained 3D porous architecture can afford fast

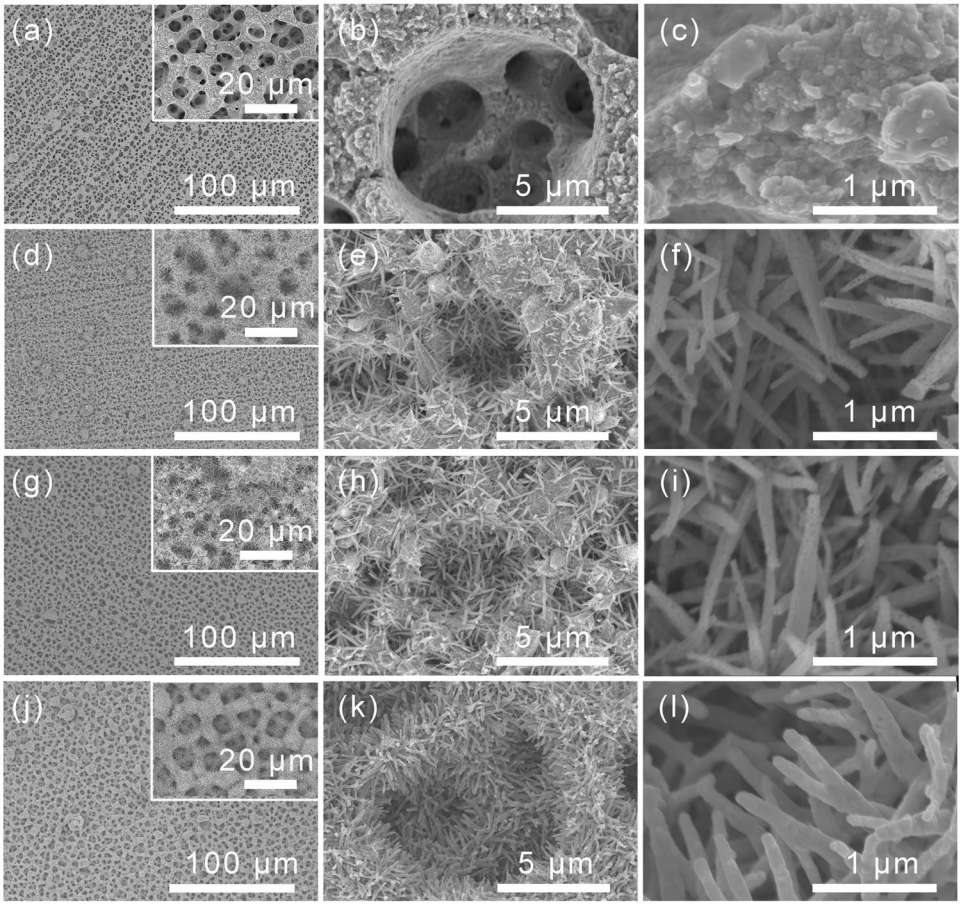

Figure 3. SEM images of 3D porous Cu after anodizing at a–c) −0.3 V (vs Hg/HgO), d–f) −0.2 V, and g–i) −0.1 V, and j–l) 0 V coupled with subsequent high temperature treatment and reduction.

transfer channels for sodium ions and free space for the volumetric variation of Sb during electrochemical cycling. Meanwhile, the Cu nanowire arrays can also provide rapid transfer channels for electrons and sodium ions. **Figure 5**a,b shows that the Sb@3D Cu NWAs replicates the morphology of 3D Cu NWAs with 3D porous structure and uniform nanowires. The side view of Sb@3D Cu NWAs (Figure 5c) indicates the whole electrode shows a thickness of about 67 μm, consisting of a uniform layer of Sb@3D Cu NWAs with about 44 μm thickness and interconnected pores. As shown in Figure 5d,e, the

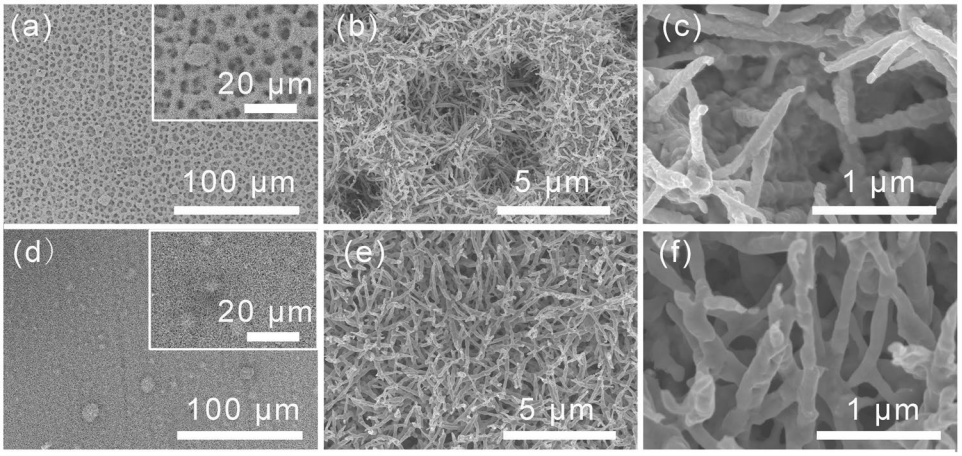

Figure 4. SEM images of 3D Cu NWAs achieved by anodizing at 0 V (vs HgO/Hg) coupled with subsequent high temperature treatment and reduction for a–c) 10 s and d–f) 40 s.

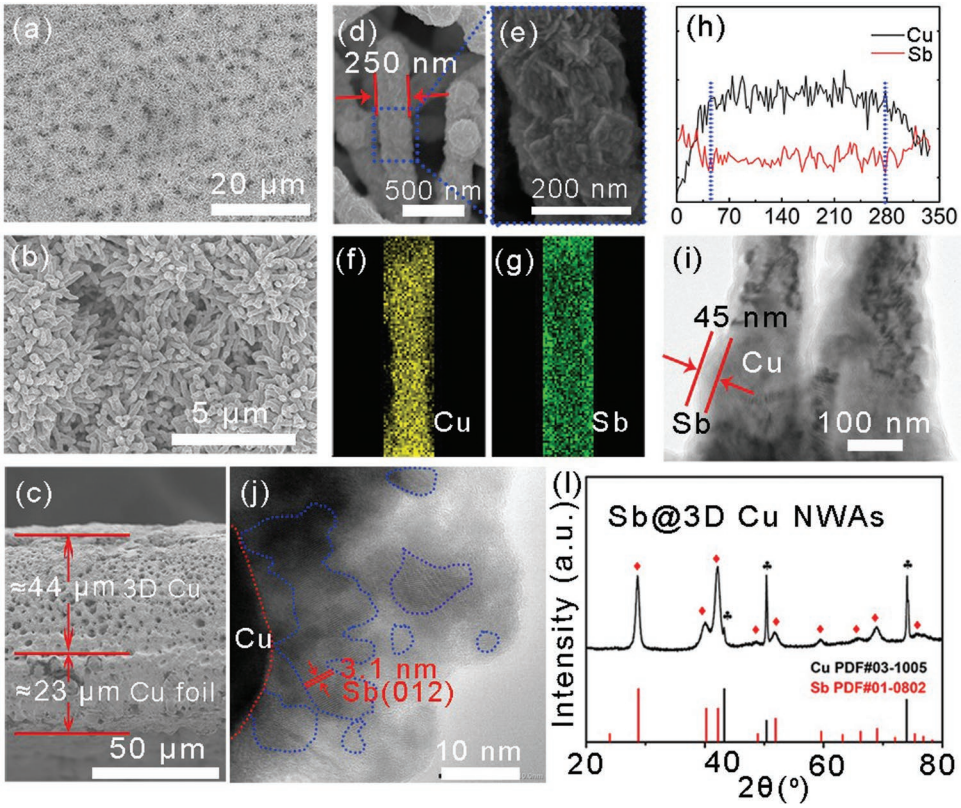

Figure 5. SEM images of Sb@3D Cu NWAs from a,b) a top view and c) side view, d) energy dispersive X-ray spectroscopy maps for elements e) Cu and f) Sb and g) corresponding line scan profile. h) TEM image and i) XRD patterns of Sb@3D Cu NWAs.

Sb nanoparticles are homogeneously coated on the Cu nanowires. This architecture is beneficial for loading more active materials and rapid transport for sodium ions. The energy-dispersive X-ray spectroscopy (EDS) mapping image for a single Sb@Cu nanowire (Figure 5f,g) confirms that Sb element is uniformly coated on the Cu nanowires. It can be determined from the EDS line scan profile (Figure 5h) that the thickness of Sb film on the Cu nanowires is about 45 nm, which is confirmed by the transmission electron microscope (TEM) image (Figure 5i). High resolution transmission electron microscope image (Figure 5j) shows that there are many nanocrystals with spacing 3.1 nm for lattice plane (012) of Sb distributed in amorphous Sb phase, indicating the low crystallinity of the prepared Sb@3D Cu NWAs.

As shown in the X-ray diffraction (XRD) patterns of the Sb@3D Cu NWAs (Figure 5l), all diffraction peaks can be assigned to crystalline Sb (The Joint Committee on Powder Diffraction Standards (JCPDS) Card No. 01-0802) besides Cu phase (JCPDS Card No. 03-1005). Scanning electron microscope (SEM) images of Sb@Cu, Sb@3D Cu, and Sb@Cu NWAs are shown in Figure S4 in the Supporting Information. The Sb@Cu displays Sb nanoparticles deposited on 2D Cu foil surface (Figure S4a–c, Supporting Information). The Sb@3D Cu demonstrates Sb nanoparticles deposited on the pore walls of 3D porous Cu (Figure S4d–f, Supporting Information). Sb@Cu NWAs show Sb nanoparticles deposited on the Cu nanowires and voids between them (Figure S4g–i, Supporting Information). XRD patterns of Sb@Cu, Sb@3D Cu, and Sb@Cu NWAs are given in Figure S5 in the Supporting Information. They also show main diffraction peaks from crystalline Sb (JCPDS Card No. 01-0802) besides Cu substrate phase (JCPDS Card No. 03-1005).

To probe the synergetic effect of the 3D porous and nanowire arrays structures on the Na storage performance of Sb, the electrochemical performance of Sb@3D Cu NWAs, Sb@Cu, Sb@3D Cu, and Sb@Cu NWAs electrodes are compared as well. In the first discharge of Sb@3D Cu NWAs electrode (**Figure 6**a and Figure S6, Supporting Information), there appears a voltage slope above 0.48 V and almost disappears since the second cycle, ascribing to electrolyte decomposition ascribed to the large specific area for this architecture.[13] Besides, there is also a short discharge voltage plateau around 0.48 V and a long discharge voltage plateau at 0.15 V, presenting appearance of amorphous Na_xSb, subsequently Na_3Sb(hexagonal)/Na_3Sb(cubic), and lastly Na_3Sb(hexagonal).[14] The first discharge (sodiation) and charge (desodiation) capacities at 100 mA g^{-1} are determined to be 1077.3 and 693.0 mAh g^{-1}, respectively, with first coulombic efficiency of 64.3%. The coulombic efficiency rapidly increases to higher than 95% since the second cycle. The first irreversible capacity mainly comes from SEI film formed from the decomposition of electrolyte on the electrode surface. Here, high reaction active points of Sb@3D Cu NWAs cause more electrolyte decomposition, thus resulting in low first coulombic efficiency. Since the second discharge, both voltages plateaus positively shift to 0.51 and 0.24 V, respectively, demonstrating a decrease of electrochemical polarization after one cycle of

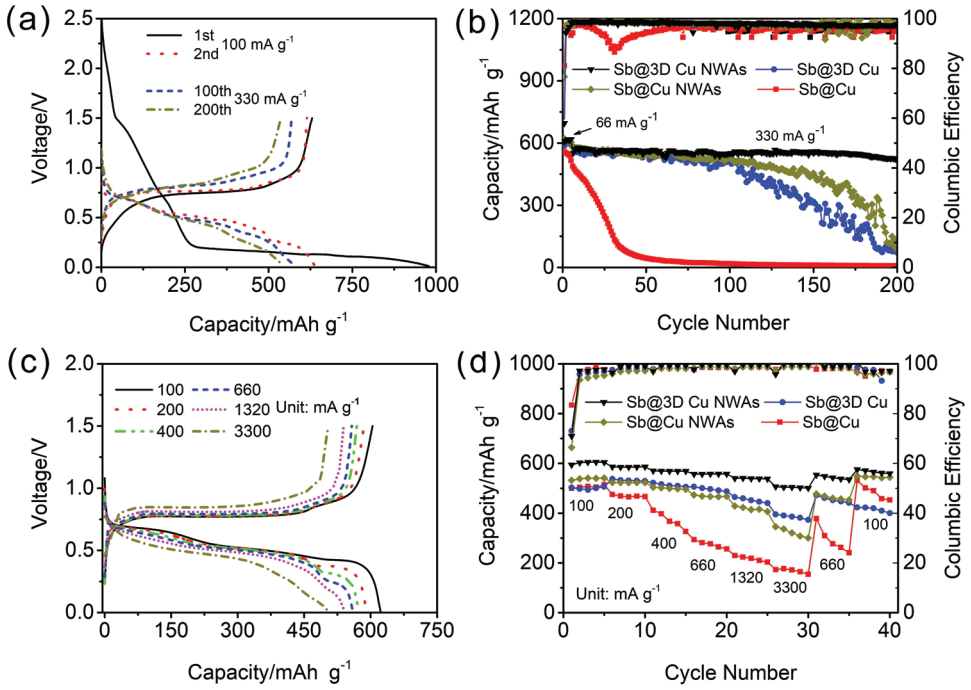

Figure 6. a) Galvanostatic discharge/charge profiles of 3D Cu NWAs electrode at 66 mA g^{-1} (1st and 2nd) and 330 mA g^{-1} (100th and 200th). b) Cyclability curves of Sb@Cu, Sb@3D Cu, and Sb@3D Cu NWAs electrodes at 330 mA g^{-1}. c) Galvanostatic discharge/charge curves of Sb@3D Cu NWAs electrode at different current densities from 0.1 to 3.3 A g^{-1}. d) Cyclability curves of Sb@Cu, Sb@3D Cu, and Sb@3D Cu NWAs electrodes at different current densities from 0.1 to 3.3 A g^{-1}.

activation. Besides, there appears a new voltage plateau at 0.68 V, may cause from the structural transformation of Sb from a hexagonal crystalline phase into an amorphous phase with Na partially remaining.[10c,15] After 200 cycles, the discharge voltage plateaus almost remain stable, signifying good electrochemical and structural stability for this architecture. For comparison, the galvanostatic discharge/charge curves of the Sb@Cu, Sb@3D Cu and Sb@Cu NWAs electrodes with their corresponding differential capacity curves are also given in Figure S7 in the Supporting Information. They show similar charge/discharge voltage curves to those of Sb@3D Cu NWAs electrode in initial two cycles. However, the capacity of Sb@Cu electrode almost decays to 0 after 100th cycles (Figure S7a, Supporting Information). Although the Sb@3D Cu and Sb@Cu NWAs electrodes still show high capacity retention in the 100th cycle, the voltage plateaus appear obvious changes. After 200 cycles, the Sb@3D Cu (Figure S7c, Supporting Information) and Sb@Cu NWAs (Figure S7e, Supporting Information) electrodes show very low capacities with voltage plateaus being seriously distorted.

Figure 6b compares the cyclability of Sb@3D Cu NWAs electrode with those of Sb@Cu, Sb@3D Cu, and Sb@Cu NWAs. The current density of initial five cycles is set as 66 mA g^{-1} and the following cycles are set as 330 mA g^{-1}. The Sb@3D Cu NWAs electrode shows an first reversible capacity of 605.3 mAh g^{-1} with an ultrahigh retention of 92.7% over 200 cycles at 330 mAh g^{-1} (561.1 mAh g^{-1} remained), which shows much better performance than those of Sb@Cu, Sb@3D Cu, and Sb@Cu NWAs electrodes. The Sb@Cu electrode can only stably charge/discharge for 20 cycles and rapidly decrease to 7.6 mAh g^{-1} in the 200th cycle. The Sb@3D Cu and Sb@Cu NWAs electrodes show better cyclability than that of Sb@Cu electrodes; however, their capacities still rapidly decrease after 100 cycles, only remaining 93.5 and 79.7 mAh g^{-1}, respectively. Besides, the Sb@3D Cu NWAs electrode demonstrates much better rate performance than those of Sb@Cu, Sb@3D Cu, and Sb@Cu NWAs electrodes. When the current densities increase from 100 to 1320 mA g^{-1}, the charge/discharge profiles of Sb@3D Cu NWAs electrode remain little change, revealing a negligible electrochemical polarization (Figure 6c). The voltage curves only display a little shift and a high reversible capacity of 554.6 mAh g^{-1} with a high retention of 84.8% compared with that at 100 mA g^{-1} even the current density increases to a higher value of 3300 mA g^{-1}. The Sb@3D Cu and Sb@Cu NWAs electrodes show similar rate performance, respectively, remaining 365.7 and 352.9 mAh g^{-1} at 3300 mA g^{-1}, which is better than that of Sb@Cu, but inferior to that of Sb@3D Cu NWAs (Figure 6d). According to the above results, the Sb@3D Cu NWAs electrode shows the best electrochemical performance, indicating the Sb electrode with 3D NWAs structure is better than those of the Sb electrodes with sole 3D porous or NWAs structure.

Such superior Na storage capacity and cycle stability of Sb@3D Cu NWAs might be ascribed to its unique 3D NWAs framework. As shown in the suggesting Na storage mechanism (**Figure 7**a,b), this architecture can provide two Na^+ transfer channels, which are a 3D porous structure from 3D Cu and interspace between nanowire arrays. Besides, the architecture can provide free space for accommodating volume changes during Na storage.[16] To further seek the effect mechanism of

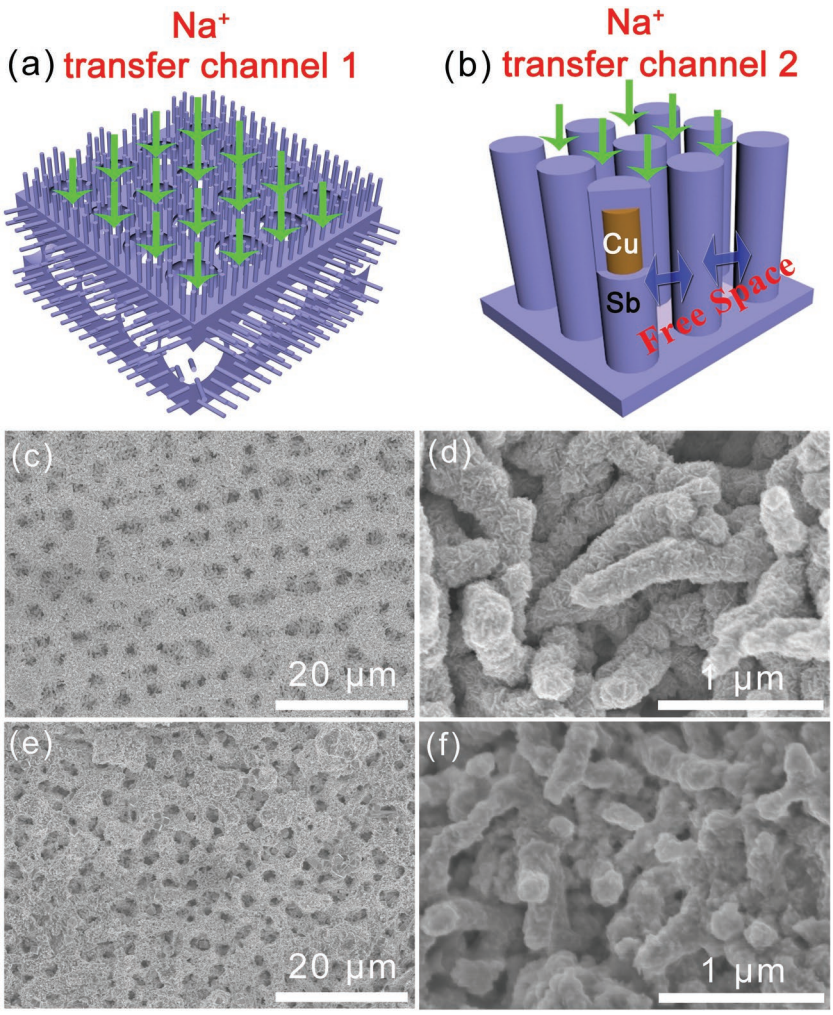

Figure 7. a,b) Na storage mechanism of Sb@3D Cu NWAs and its SEM images suffered c,d) 1 and e,f) 200 cycles.

3D NWAs structure on the electrochemical Na storage performance in Sb, the SEM images of Sb@3D Cu NWAs suffered 1 and 200 cycles are characterized and given in Figure 7c–f. After one electrochemical cycle, the surface of nanowires become rougher, and the 3D porous and array structures remain well (Figure 7c,d). After 200 cycles, there appears somewhat aggregation of nanowires but the 3D porous structure remains well, resulting in a little capacity decrease appears after 200 cycles. For comparison, the Sb@Cu surface becomes dense and no Na^+ transfer channels and free space for accommodating volume changes after 200 cycles (Figure S8a–c, Supporting Information). The Sb@3D Cu keeps some macropores however the Sb particles appear serious aggregation, causing a block for Na^+ transport (Figure S8d–f, Supporting Information). The Sb@Cu NWAs electrode shows serious aggregation of nanowires, blocking the Na^+ transfer channels (Figure S8g–i, Supporting Information). Therefore, the Sb@3D Cu NWAs demonstrates much better electrochemical cycling and rate capacity than those of the Sb@Cu, Sb@3D Cu, and Sb@Cu NWAs electrodes.

To further understand the electrochemical performance revolution, we have also tested the electrochemical impedance spectra of Sb@Cu, Sb@3D Cu, Sb@Cu NWAs, and Sb@3D Cu NWAs suffered 6 and 100 cycles, and their Nyquist plots are shown in **Figure 8**. They all include an arc in the high frequency region and a straight line in the low frequency region. The high frequency arc is related to electrochemical reaction impedance, the low frequency straight line presents Na ions diffusion impedance in active particles. It can be observed that the Sb@3D Cu NWAs electrode has the smallest high frequency arc in the 6th cycle, indicating the lowest electrochemical reaction impedance. After 100 cycles, the high frequency arc appears almost no change, demonstrating stable electrode/electrolyte interphase. For comparison, high frequency arcs of Sb@Cu, Sb@3D Cu, and Sb@Cu NWAs in the 6th cycle decrease in sequence. The high frequency arc of Sb@Cu increases the most after 100 cycles, that of Sb@Cu NWAs increase the least but larger than that of Sb@3D Cu NWAs. These results are in good agreement with their electrochemical performance revolution.

To investigate the practical use of Sb@3D Cu NWAs electrode, it was coupled with $Na_3V_2(PO_4)_3/C$ cathode for a full cell of SIBs. The mass loading ratio between cathode and anode is kept at 5:1 (the whole loading of the cathode is about 3 mg). The $Na_3V_2(PO_4)_3/C$ shows a first capacity of 98 mAh g^{-1} with a columbic efficiency of 94.84% at 600 mA g^{-1} (about 5C, 1C = 117 mA g^{-1}) in half-cell, and high capacity retention of 96% after 500 cycles (Figure S9, Supporting Information). The full cell is evaluated at 117 mA g^{-1} with the voltage range from 1.8 to 4 V according to the charge/discharge curves of Sb@3D Cu NWAs and $Na_3V_2(PO_4)_3/C$, respectively (**Figure 9**a). The

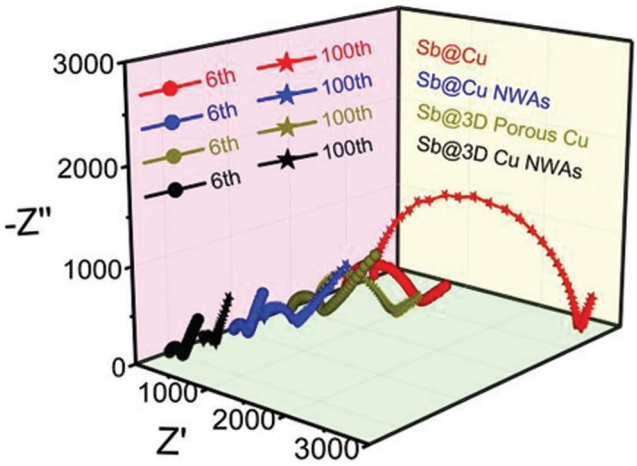

Figure 8. The Nyquist plots of Sb@Cu, Sb@3D Cu, Sb@Cu NWAs, and Sb@3D Cu NWAs.

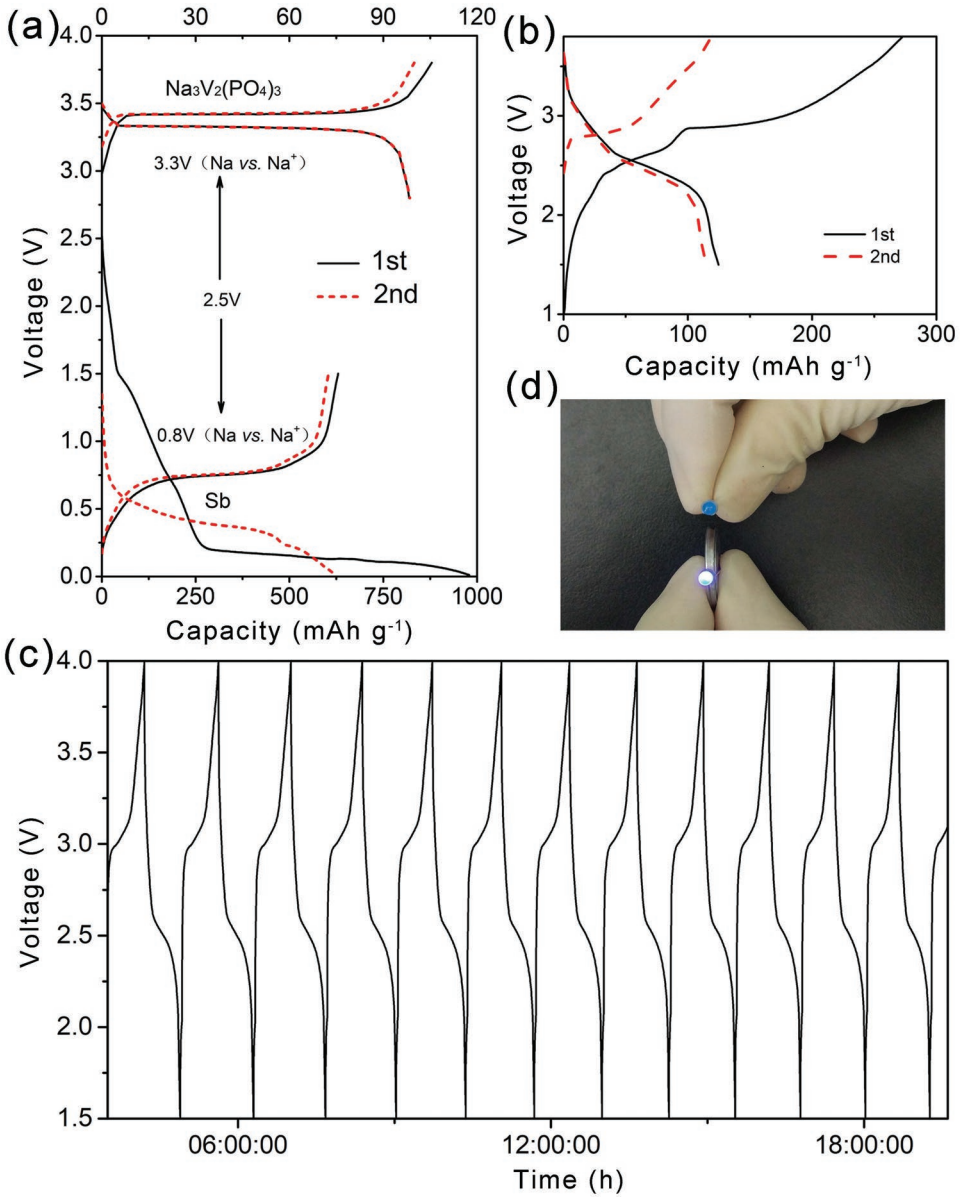

Figure 9. Electrochemical performance of Sb@3D Cu NWAs//$Na_3V_2(PO_4)_3$ full cells. a) The first and second galvanostatic charge–discharge curves of Sb@3D Cu NWAs and $Na_3V_2(PO_4)_3$, respectively, and b) the full cell assembled by them. c) Typical galvanostatic charge–discharge profiles of the full cell at a current density of 120 mA g^{-1} (based on the anode). d) A LED bulb powered by the full cell.

full battery delivers two flat charge voltage plateaus around 2.5 and 2.8 V, respectively, and a discharge plateau around 2.5 V (Figure 9b), stable cyclability (Figure 9c), and an energy density of 263 Wh kg^{-1} (based on whole mass loading of cathode and anode), which can power an light emitting diode (LED) bulb (Figure 9d).

3. Conclusions

In summary, we design and produce a controllable 3D current collector assembled from 1D Cu nanowire arrays anchored on 3D porous Cu (3D Cu NWAs) through anodizing and subsequent high-temperature reduction. Element Sb is electrodeposited on the 3D Cu NWAs and directly served as the anode of SIBs. This unique architecture combines the advantages of 1D nanowire array (near 150–200 nm) and 3D porous (about 5 μm) structures, benefiting to electron and Na^+ rapid transport and accommodating volume variation during Na storage cycling. Thus, the Sb@3D Cu NWAs electrode exhibits a high reversible capacity of 605.3 mAh g^{-1} at 330 mA g^{-1} with 561.1 mAh g^{-1} remained after 200 cycles (the capacity retention is 92.7%). In addition, it manifests a high reversible capacity of 554.6 mAh g^{-1} with a high retention of 84.8% compared with that at 100 mA g^{-1} even at a high current density of 3300 mA g^{-1}. The full cell assembled using Sb@3D NWAs electrode as anode and $Na_3V_2(PO_4)_3$/C as cathode shows high energy density of 263 Wh kg^{-1}. Since simplicity and effectiveness, this proposed electrode design may

direct a new road to construct electrode frameworks for high-performance batteries.

4. Experimental Section

Synthesis of 3D Cu Nanowire Arrays: All reagents used are analytically pure. The 3D porous Cu was prepared via an electroless plating strategy as reported in our previous work involving two reactions, $H_2PO_2^- + Ni^{2+} + OH^- \rightarrow Ni + HPO_3^{2+} + H_2$, $H_2PO_2^- + Cu^{2+} + OH^- \rightarrow Cu + HPO_3^{2+} + H_2$,[17] respectively. Ni^{2+} acts as a catalyst to assure the continuously reduction of Cu^{2+} to metallic Cu layer, growing on the substrate and remained in the 3D porous Cu layer. LSV was performed to determine the anodizing electrode potential for preparing 3D Cu nanowire arrays. In a typical process, LSV was carried out on an electrochemical workstation (Princeton, VersaSTAT 3) using a scanning rate of 1 mV s^{-1} from open circuit potential (about –0.5 V vs Hg/HgO) to 1.0 V (vs Hg/HgO). The electrolyte is 240 g L^{-1} NaOH, work electrode is 3D porous Cu, auxiliary electrode is Pt@Ti mesh and reference electrode is Hg/HgO. To better understand the electrochemical reactions involved in the anodizing processes on 3D porous Cu, the LSV curves of Cu and Ni foils were also tested in the same LSV condition. According to the LSV curve of 3D porous Cu, –0.3, –0.2, –0.1, 0, 0.2, 0.6, and 1.0 V were chosen as the anodizing electrode potentials to determine the promising potential for preparing 3D Cu nanowire arrays. Besides, the anodizing time of 10, 20, and 40 s was also chosen to determine the promising time. After anodizing, the samples were treated at 400 °C for 2 h in pure Ar followed by 200 °C for 4 h in Ar/H_2 (95/5) flow. Based on the SEM images of these samples after anodizing at different electrode potentials for different time, the sample achieved at 0 V for 20 s has the ideal architecture as the current density and denoted as 3D NWAs.

Synthesis of Sb@3D Cu Nanowire Arrays: Sb@3D Cu nanowire arrays (denoted as Sb@3D Cu NWAs) were synthesized by electrodeposition at a constant current density of 5.0 mA cm^{-2} for 200 s in an electrodeposition bath containing 6 g L^{-1} Sb_2O_3, 80 g L^{-1} $C_6H_8O_7{\cdot}2H_2O$, 100 g L^{-1} $Na_3C_6H_5O_7$, and 3 g L^{-1} $C_6H_5CO_2Na$. In the electrodeposition system, 3D Cu NWAs were served as working electrode and Pt@Ti mesh as the counter electrode. For comparison, Sb film was electrodeposited on Cu foil, 3D porous Cu, and Cu nanowire arrays in the same condition and denoted as Sb@Cu, Sb@3D Cu, and Sb@Cu NWAs, respectively. The corresponding mass loading of all the electrodes is in the range of 0.5–0.6 mg cm^{-2}.

Materials Characterization: The electrode morphology was characterized by SEM (Hitachi S4800, Japan) and TEM (JEM-2100, Japan). The crystalline structure was measured by XRD with Cu K_α radiation ($\lambda = 0.15406$ nm).

Electrochemical Characterization: Electrochemical performance of Sb@3D Cu NWAs in half-cell using 2025 type coin cells was tested on the LAND battery test system (CT2001A) in the voltage range from 0.01 to 1.5 V (vs Na^+/Na) at different current densities. Coin cells were assembled with Sb@3D Cu NWAs as the positive electrodes, Na sheet (homemade) as the negative electrode, glass fiber filter paper (Whatman GF/D) as the separator, $NaClO_4$ (1 mol L^{-1}) dissolved in ethylene carbonate and dimethyl carbonate (1:1 by volume, provided by Qianmin Chemical Reagent co. LTD, Su Zhou, China) with 5% fluoroethylene carbonate as the electrolyte. The full battery assembled with Sb@3D Cu NWAs as anode and $Na_3V_2(PO_4)_3$ as cathode was tested in the voltage range from 1.5 to 4 V. The cycling performance of $Na_3V_2(PO_4)_3$ in half-cell was tested at 600 mA g^{-1} (≈5 C) in the voltage range between 2.8 and 3.8 V. The electrochemical impedance spectra are performed on electrochemical work station (Preston, VersaSTAT 3) at 0.5 V with amplitude of 5 mV and frequency range of 10^5–10^{-2} Hz.

Supporting Information

Supporting Information is available from the Wiley Online Library or from the author.

Acknowledgements

This research was financial supported by the National Natural Science Foundation of China (No. 21473014), the Natural Science Foundation of Shaanxi Province of China (2016JM2024), the China Postdoctoral Science Foundation (2016M590908), the Special Fund for Basic Scientific Research of Central Colleges, Chang'an University, China (Grant No. 310831153505).

Conflict of Interest

The authors declare no conflict of interest.

Keywords

3D current collectors, alloying anodes, nanowires, sodium ion batteries

Received: February 26, 2019
Revised: April 28, 2019
Published online: June 6, 2019

[1] a) L. Smith, B. Dunn, *Science* **2015**, *350*, 918; b) D. Gielen, F. Boshell, D. Saygin, *Nat. Mater.* **2016**, *15*, 117; c) H. Pan, Y.-S. Hu, L. Chen, *Energy Environ. Sci.* **2013**, *6*, 2338; d) S. P. Ong, V. L. Chevrier, G. Hautier, A. Jain, C. Moore, S. Kim, X. Ma, G. Ceder, *Energy Environ. Sci.* **2011**, *4*, 3680.

[2] a) J. W. Choi, D. Aurbach, *Nat. Rev. Mater.* **2016**, *1*, 16013; b) R. Raccichini, A. Varzi, S. Passerini, B. Scrosati, *Nat. Mater.* **2015**, *14*, 271; c) B. L. Ellis, L. F. Nazar, *Curr. Opin. Solid State Mater. Sci.* **2012**, *16*, 168.

[3] a) S.-W. Kim, D.-H. Seo, X. Ma, G. Ceder, K. Kang, *Adv. Energy Mater.* **2012**, *2*, 710; b) V. Palomares, P. Serras, I. Villaluenga, K. B. Hueso, J. Carretero-González, T. Rojo, *Energy Environ. Sci.* **2012**, *5*, 5884.

[4] a) A. Ponrouch, E. Marchante, M. Courty, J.-M. Tarascon, M. R. Palacín, *Energy Environ. Sci.* **2012**, *5*, 8572; b) M. D. Slater, D. Kim, E. Lee, C. S. Johnson, *Adv. Funct. Mater.* **2013**, *23*, 947; c) J. Y. Hwang, S. T. Myung, Y. K. Sun, *Chem. Soc. Rev.* **2017**, *46*, 3529.

[5] a) T.-S. Wang, Y. Liu, Y.-X. Lu, Y.-S. Hu, L.-Z. Fan, *Energy Storage Mater.* **2018**, *15*, 274; b) Q. Wei, F. Xiong, S. Tan, L. Huang, E. H. Lan, B. Dunn, L. Mai, *Adv. Mater.* **2017**, *29*, 1602300; c) C. Chen, K. Fu, Y. Lu, J. Zhu, L. Xue, Y. Hu, X. Zhang, *RSC Adv.* **2015**, *5*, 30793; d) Y. Lu, Z. Tu, L. A. Archer, *Nat. Mater.* **2014**, *13*, 961; e) Y. Cao, L. Xiao, M. L. Sushko, W. Wang, B. Schwenzer, J. Xiao, Z. Nie, L. V. Saraf, Z. Yang, J. Liu, *Nano Lett.* **2012**, *12*, 3783; f) S. Liu, J. Feng, X. Bian, J. Liu, H. Xu, *Energy Environ. Sci.* **2016**, *9*, 1229.

[6] a) J. Qin, T. Wang, D. Liu, E. Liu, N. Zhao, C. Shi, F. He, L. Ma, C. He, *Adv. Mater.* **2018**, *30*, 1704670; b) L. Baggetto, P. Ganesh, C.-N. Sun, R. A. Meisner, T. A. Zawodzinski, G. M. Veith, *J. Mater. Chem. A* **2013**, *1*, 7985; c) H. Li, K. Wang, S. Cheng, K. Jiang, *ACS Appl. Mater. Interfaces* **2016**, *8*, 12830; d) G. Tan, F. Wu, Y. Yuan, R. Chen, T. Zhao, Y. Yao, J. Qian, J. Liu, Y. Ye, R. Shahbazian-Yassar, J. Lu, K. Amine, *Nat. Commun.* **2016**, *7*, 11774; e) H. Xie, W. P. Kalisvaart, B. C. Olsen, E. J. Luber, D. Mitlin, J. M. Buriak, *J. Mater. Chem. A* **2017**, *5*, 9661.

[7] a) J. Qian, Y. Chen, L. Wu, Y. Cao, X. Ai, H. Yang, *Chem. Commun.* **2012**, *48*, 7070; b) W. Luo, P. Zhang, X. Wang, Q. Li, Y. Dong, J. Hua, L. Zhou, L. Mai, *J. Power Sources* **2016**, *304*, 340; c) X. Zhang, P. Li, R. Zang, S. Wang, Y. Zhu, C. Li, G. Wang, *Chem.* -

Asian J. **2017**, *12*, 116; d) T. Wu, C. Zhang, H. Hou, P. Ge, G. Zou, W. Xu, S. Li, Z. Huang, T. Guo, M. Jing, X. Ji, *Adv. Funct. Mater.* **2018**, *28*, 1705744; e) G. Wang, X. Xiong, Z. Lin, C. Yang, Z. Lin, M. Liu, *Electrochim. Acta* **2017**, *242*, 159; f) X. Zhou, Z. Dai, J. Bao, Y.-G. Guo, *J. Mater. Chem. A* **2013**, *1*, 13727.

[8] a) S. Dong, C. Li, Z. Li, L. Zhang, L. Yin, *Small* **2018**, *14*, 1704517; b) N. Wang, Z. Bai, Y. Qian, J. Yang, *ACS Appl. Mater. Interfaces* **2017**, *9*, 447.

[9] a) H. Hou, M. Jing, Z. Huang, Y. Yang, Y. Zhang, J. Chen, Z. Wu, X. Ji, *ACS Appl. Mater. Interfaces* **2015**, *7*, 19362; b) D. H. Nam, K. S. Hong, S. J. Lim, M. J. Kim, H. S. Kwon, *Small* **2015**, *11*, 2885; c) W. Luo, A. Calas, C. Tang, F. Li, L. Zhou, L. Mai, *ACS Appl. Mater. Interfaces* **2016**, *8*, 35219; d) C. Xu, J. Liao, C. Yang, R. Wang, D. Wu, P. Zou, Z. Lin, B. Li, F. Kang, C.-P. Wong, *Nano Energy* **2016**, *30*, 900.

[10] a) L. Bodenes, A. Darwiche, L. Monconduit, H. Martinez, *J. Power Sources* **2015**, *273*, 14; b) M. Lao, Y. Zhang, W. Luo, Q. Yan, W. Sun, S. X. Dou, *Adv. Mater.* **2017**, *29*, 1700622; c) A. Darwiche, C. Marino, M. T. Sougrati, B. Fraisse, L. Stievano, L. Monconduit, *J. Am. Chem. Soc.* **2012**, *134*, 20805; d) X.-Y. Fan, J. Han, Y. Jiang, J. Ni, L. Gou, D.-L. Li, L. Li, *ACS Appl. Energy Mater.* **2018**, *1*, 3598.

[11] a) J. Hur, I. T. Kim, *Bull. Korean Chem. Soc.* **2015**, *36*, 1625; b) Y. Yang, X. Yang, Y. Zhang, H. Hou, M. Jing, Y. Zhu, L. Fang, Q. Chen, X. Ji, *J. Power Sources* **2015**, *282*, 358; c) Z. Li, X. Tan, P. Li, P. Kalisvaart, M. T. Janish, W. M. Mook, E. J. Luber, K. L. Jungjohann, C. B. Carter, D. Mitlin, *Nano Lett.* **2015**, *15*, 6339.

[12] a) J. Ni, Y. Jiang, F. Wu, J. Maier, Y. Yu, L. Li, *Adv. Funct. Mater.* **2018**, *28*, 1707179; b) C. P. Yang, Y. X. Yin, S. F. Zhang, N. W. Li, Y. G. Guo, *Nat. Commun.* **2015**, *6*, 8058; c) S. Yuan, X. L. Huang, D. L. Ma, H. G. Wang, F. Z. Meng, X. B. Zhang, *Adv. Mater.* **2014**, *26*, 2273.

[13] L. Ji, M. Gu, Y. Shao, X. Li, M. H. Engelhard, B. W. Arey, W. Wang, Z. Nie, J. Xiao, C. Wang, J. G. Zhang, J. Liu, *Adv. Mater.* **2014**, *26*, 2901.

[14] a) L. Liang, Y. Xu, C. Wang, L. Wen, Y. Fang, Y. Mi, M. Zhou, H. Zhao, Y. Lei, *Energy Environ. Sci.* **2015**, *8*, 2954; b) X. Zhou, Y. Zhong, M. Yang, M. Hu, J. Wei, Z. Zhou, *Chem. Commun.* **2014**, *50*, 12888.

[15] H. Hou, M. Jing, Y. Yang, Y. Zhang, Y. Zhu, W. Song, X. Yang, X. Ji, *J. Mater. Chem. A* **2015**, *3*, 2971.

[16] a) X. Liu, D. Chao, D. Su, S. Liu, L. Chen, C. Chi, J. Lin, Z. X. Shen, J. Zhao, L. Mai, Y. Li, *Nano Energy* **2017**, *37*, 108; b) H. Shang, Z. Zuo, L. Li, F. Wang, H. Liu, Y. Li, Y. Li, *Angew. Chem., Int. Ed.* **2018**, *57*, 774; c) J. Qian, W. A. Henderson, W. Xu, P. Bhattacharya, M. Engelhard, O. Borodin, J. G. Zhang, *Nat. Commun.* **2015**, *6*, 6362.

[17] X.-Y. Fan, Y.-X. Shi, Y. Cui, D.-L. Li, L. Gou, *Ionics* **2015**, *21*, 1909.